Modeling neutral beam deposition and fast ion orbit loss on EAST tokamak with three-dimensional external magnetic perturbations

by Youjun Hu[1,2,*], Baolong Hao[1], Yongjian Xu[1], Yinfeng Xu[1], Bin Wu[1]

1. Institute of Plasma Physics, Chinese Academy of Sciences, Hefei 230031, China
2. Center for Magnetic Fusion Theory, Chinese Academy of Sciences, Hefei, Anhui 230031, China
*Email: yjhu@ipp.cas.cn

Abstract

A Monte-Carlo code was developed to calculate the neutral beam ionization and fast ions orbit loss under the influence of the three-dimensional external magnetic perturbations on the Experimental Advanced Superconducting Tokamak (EAST).

1 Introduction

Heating tokamak plasma by injecting beams of energetic neutral particles is widely adopted in contemporary tokamaks[1, 2, 3, 4, 5]. Since the injected particles are neutral, they are not influenced by the strong magnetic field of tokamaks, which makes it easy for them to enter the plasma. After entering the plasma, the neutral particles encounter collisions with ions and electrons of the background plasma, which makes them ionize and thus become fast ions. These fast ions then move under the influence of the strong magnetic field of tokamaks. The fast ions needs to stay within the plasma for a long time (of slowing-down time scale, $\sim$100ms for typical parameters of contemporary tokamak) to efficiently heat the thermal plasma through collision with the thermal ions and electrons. However, some fast ions are quickly lost to the wall of the device after their birth because their orbits touch the wall. This kind of loss is usually called prompt loss or orbit loss[6]. Whether a fast ions is prompt lost depends on its velocity and birth location in the plasma. To estimate the fraction of fast ions that are prompt lost for a specific neutral beam injection (NBI) and a specific thermal plasma configuration, one needs to calculate the ionization process, which determines the birth location of the fast ions, and the fast ions orbit to determine whether the trajectories touch the wall. This paper reports the results of this kind of calculations, which are performed for the Experimental Advanced Superconducting Tokamak (EAST) located in Hefei city and managed by Institute of Plasma Physics, Chinese Academy of Sciences. EAST is equipped with coils that can produce three-dimensional (3D) magnetic perturbations, which are often called Resonant Magnetic Perturbation (RMP) and are designed for the control of Edgy Localized Modes (ELMs)[7], but turns out to also have effects on the prompt loss of neutral beam fast ions[8]. These effects are modeled by a newly developed Monte-Carlo code `TGCO` that calculates the ionization and the prompt loss under the influence of the 3D magnetic perturbations produced by the RMP coils.

The remainder of this paper is organized as follows. Section 2 describe how to model the neutral beam source (the part that is outside tokamak vacuum vessel). Section 3 describes the method of computing the ionization process and the initial spatial distributions of the fast ions, which are compared with the results obtained from an established NBI modeling code, NUBEAM[9]. Sections 4-6 discusses the prompt loss of fast ions under the influence of the RMP coils, where the spatial distribution of the lost ions on the first wall is given. A brief summary is given in Sec. 7.

Numerical results indicate that the 3D magnetic perturbations increase the orbit loss of NBI fast ions and change the toroidal distribution of the lost ions.

2 Neutral beam source

To create beam of neutral particles of high energy for the purpose of heating tokamak plasma, one usually needs a system consisting of (1) ion source, which produces low-energy ions, (2) a set of accelerating grids, which is attached to the window of the ion-source arc-chamber, to accelerate the ions to energetic ion beam, (3) a neutralizing chamber, which neutralizes the ion beam to neutral beam, and (4) a bending magnet to remove remained charged particles from the beam. Figure 1 shows a sketch map of the accelerating grids of EAST neutral beam system.
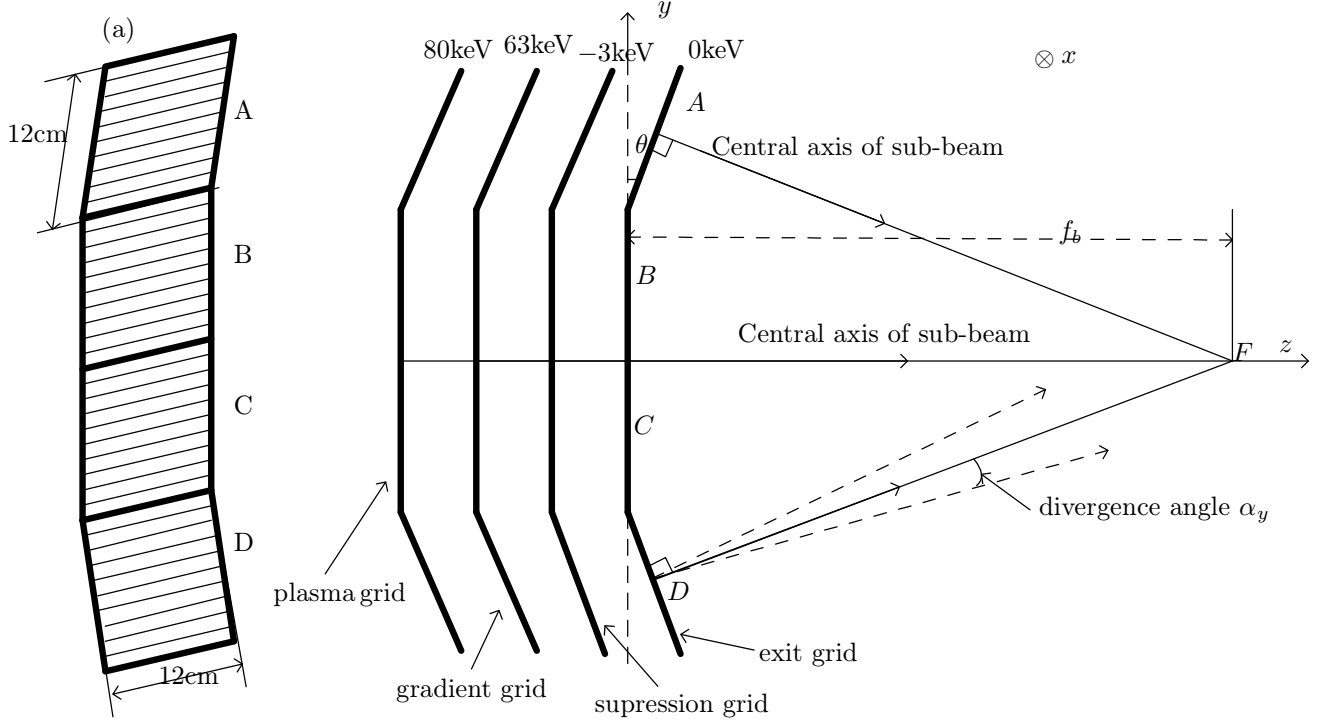

Figure 1. (a) Three-dimensional sketch map of one of the accelerating grids. (b) Side view of the four groups of accelerating grids of EAST neutral beam injector, which are called plasma grid, gradient grid, suppression grid, and exit grid, respectively. Each accelerating grid has four sub-grids, indicated by A, B, C, and D on the figure. Sub-grids A and D are rotated with respect to the central sub-grids B and C by a small angle $\theta = \left(1\frac{1}{12}\right)^\circ$. This angle is exaggerated on the figure. The central axis of the two beams from grids A and D intersect at F. The vertical focal length f_b is defined as the distance from point F to the plane of BC grids. Each sub-grid is a 12cm × 12cm square. A typical setting of the voltage on the grids is indicated on the figure. The $y = 0$ plane is assumed to be the tokamak midplane.

Neglecting the beam divergence (discussed later), a beam from a sub-electrode is perpendicular to the corresponding grid plane. As is shown in Fig. 1, two of the sub-electrodes A and D are rotated with respect to the central sub-electrodes by a small angle θ. This focuses the beams from A and D with a focal length given by

$$f_b \approx \frac{L_y}{\tan(2\theta/3)}, \tag{1}$$

where L_y is the vertical length of the sub-grid. For EAST neutral beam system, $\theta = \left(1\frac{1}{12}\right)^\circ$ and $L_y = 0.12m$, Eq. (1) gives that the focal length $f_b \approx 9.52m$. To efficiently utilize the beam, the distance between the accelerating grids and the tokamak plasma is chosen to be approximately equal to the above focal length, i.e. $\approx 9m$.

The above focal length is the for the vertical plane ((y, z) plane). The horizontal focal length (on (x, z) plane) is infinity for EAST NBI because all the sub-electrodes are flat in the horizontal direction.

An important property of a beam is the beam divergence. The velocity direction of ions emitting from the exit grid usually deviates from the central axis of the beam. This deviation is called beam divergence (see Fig. 1). In the Monte-Carlo method used in this work, the beam divergence is implemented by setting the velocity direction (via setting α_y and α_x defined below) of the loaded markers at the exit grid according to the following Gaussian distributions:

$$P(\alpha_y) = \frac{1}{\sqrt{2\pi}\alpha_{y0}}\exp\left(-\frac{\alpha_y^2}{2\alpha_{y0}^2}\right), \tag{2}$$

and

$$P(\alpha_x) = \frac{1}{\sqrt{2\pi}\alpha_{x0}}\exp\left(-\frac{\alpha_x^2}{2\alpha_{x0}^2}\right), \tag{3}$$

where α_y is the angle between the beam central axis and the projection of the particle velocity in (y, z) plane, as is shown in Fig. 1, and similarly α_x is the angle between $\hat{\mathbf{z}}$ and the projection of the velocity in (x, z) plane, α_{x0} and α_{y0} are the standard deviations of the distributions, which in this case characterize the magnitude of the beam divergence. For neutral beam source on EAST, $\alpha_{x0} \approx 0.6°$ and $\alpha_{y0} \approx 1.2°$.

The above discussion addresses the velocity direction of the particles emitting from the accelerating grids. Besides the direction, we need to set the magnitude of the particle velocity (or the kinetic energy). For the EAST neutral beam system, which uses Deuteron ion-sources, a particle going through the accelerating grids can be a Deuteron (denoted by D^+), or a Deuteron combined with one or two additional Deuterium atoms (denoted by D_2^+ and D_3^+). The number ratio between D^+, D_2^+, and D_3^+ entering the accelerating grids is determined by the ion-source. All particles (D^+, D_2^+, and D_3^+) going through the accelerating grids get the same kinetic energy eU because they are all single-charged and passing through the same voltage drop, where e being the elementary charge and U the voltage drop on the accelerating grids. These charged particles then pass through the neutralizing chamber, which neutralizes the ion beam to a neutral beam. The neutralizing efficiency depends on the velocity of the particles. Since the velocity of D^+, D_2^+, and D_3^+ is different from each other, the ratio between the corresponding neutralized single-atom, bi-atom, trip-atom particles (denoted by D, D_2, and D_3, respectively) is changed from the ratio between D^+, D_2^+, and D_3^+ emitting from the accelerating grids. The kinetic energy of D_2 and D_3 is divided equally by their components atom when they separate from each other, which generates single-atom particles of kinetic energy $E_{\text{full}}/2$, and $E_{\text{full}}/3$, where $E_{\text{full}} = eU$. In the simulations, all markers loaded are considered as single-atom particles and the number ratio between particles of kinetic energy E_{full}, $E_{\text{full}}/2$, and $E_{\text{full}}/3$ is set to be $80\%{:}\,14\%{:}\,6\%$.

In simulations, kinetic energies of markers are randomly chosen among the three energies while satisfying the above number ratio between them.

The neutralizing process is not directly modeled in the simulation and its effect is included only through the input number ratio between particles with energies of E_{full}, $E_{\text{full}}/2$, and $E_{\text{full}}/3$. We assume that other beam properties (e.g. focus and divergence) are not changed by the neutralizing process, except that only part of the ions succeed in becoming neutrals and the remaining ions will be removed by the deflector magnet before they reach the tokamak vessel.

The spatial distribution of particles on the exit grid is assumed to be uniform and are implemented in the simulation via setting particle location by using a uniformly distributed random variable.

After setting all the above parameters, each marker gets a set of well-defined initial conditions, which can be used to determine its subsequent orbit, which is assumed to be along a straight line

until the marker arrives at the ionization location in the plasma. In addition, due to the finite size of the vacuum window, through which neutral particles need to pass to enter the tokamak vessel, those particles with large divergence angles can not pass through the window to enter the vessel and this effect is modeled in the simulation.

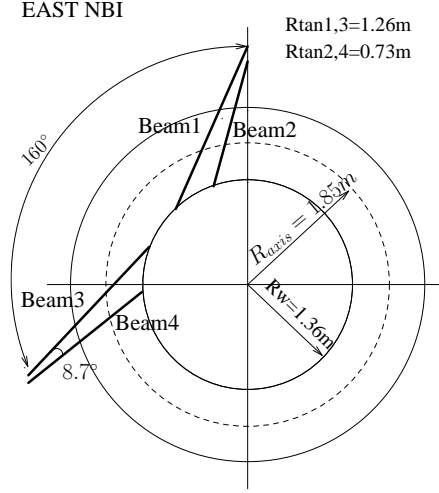Figure 2 gives the top view of the four neutral beam lines on EAST tokamak.

Figure 2. Top view of neutral beam lines on EAST tokamak. The beam tangent radius R_{tan} is defined as the perpendicular distance from the tokamak center to a beam line. A beam line is defined as the central axis perpendicular to the central accelerating grids.

3 Monte-Carlo implementation of fast ion birth from neutral particle ionization in plasma

Define ν by

$$\nu = n_i \sigma_{\mathrm{ch}} + n_i \sigma_i + n_e \frac{\langle \sigma_e v_e \rangle}{v_b}, \tag{4}$$

where n_i and n_e are, respectively, the number density of background plasma ions and electrons, σ_{ch} is the cross-section for charge exchange with plasma ions, σ_i are the cross-section for ionization by plasma ions, $\langle \sigma_e v_e \rangle$ is the electron impact ionization rate coefficient averaged over the Maxwellian distribution, $\langle \sigma_e v_e \rangle / v_b$ is the effective cross-section of electron impact ionization, where v_b is the neutral particle velocity. The ionization cross-sections data used in this work are provided in Appendix A.

The Monte-Carlo method of implementing the ionization process is as follows. First associate each marker loaded with a random number η that is uniformly distributed in $[0, 1]$. Then, along the trajectory of each neutral particle (straight line), the integration $s = \int_0^l \nu(l')dl'$ is calculated to examine whether $s \geqslant \ln(1/\eta)$ or not. If $s \geqslant \ln(1/\eta)$, then the neutral particle is considered to be ionized. The value of ν outside the last closed flux surface (LCFS) is set to be zero, i.e., the ionization outside LCFS is not considered.

The Monte-Carlo implementation gives the ionization locations of each marker loaded in the simulation. These locations are used as initial conditions in the subsequent orbit following computations. Those neutral particles that are not yet ionized when they reach the inner wall of the

device are lost to the wall and this loss are called shine-through loss.

3.1 Benchmark the new code with NUBEAM code

To verify the reliability of the new code `TGCO` in modeling the ionization process, we carried out a benchmarking with the NUBEAM code[9]. The plasma density and temperature profiles used in the benchmarking case are shown in Fig. 3. The magnetic configuration is reconstructed by EFIT code[10] from EAST experiment measurements.
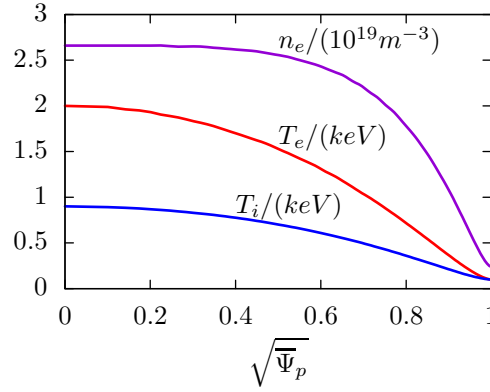

Figure 3. Profiles of electron number density , electron temperature, and ion temperature used in the benchmarking case, where the radial coordinate, $\sqrt{\overline{\Psi}_p}$, is the square root of the normalized poloidal magnetic flux. These profiles are for EAST discharge #59954@3.0s.

The ionization cross-sections (see Append. A) used in the new code `TGCO` do not include the contributions from multi-step ionization process. Multi-step ionization refers to the case where a collision push a neutral into its excited state and a subsequent collision remove the electron from the neutral before the electron decays to its ground state. NUBEAM include the excited state correction due to this multi-step ionization and this correction is turned off in the benchmarking case. Furthermore, the ionization due to collision with impurities is not included in the new code and is turned off in NUBEAM in the benchmarking case. The comparison of the beam density deposition profiles calculated by `TGCO` and NUBEAM code are shown in Fig. 4.
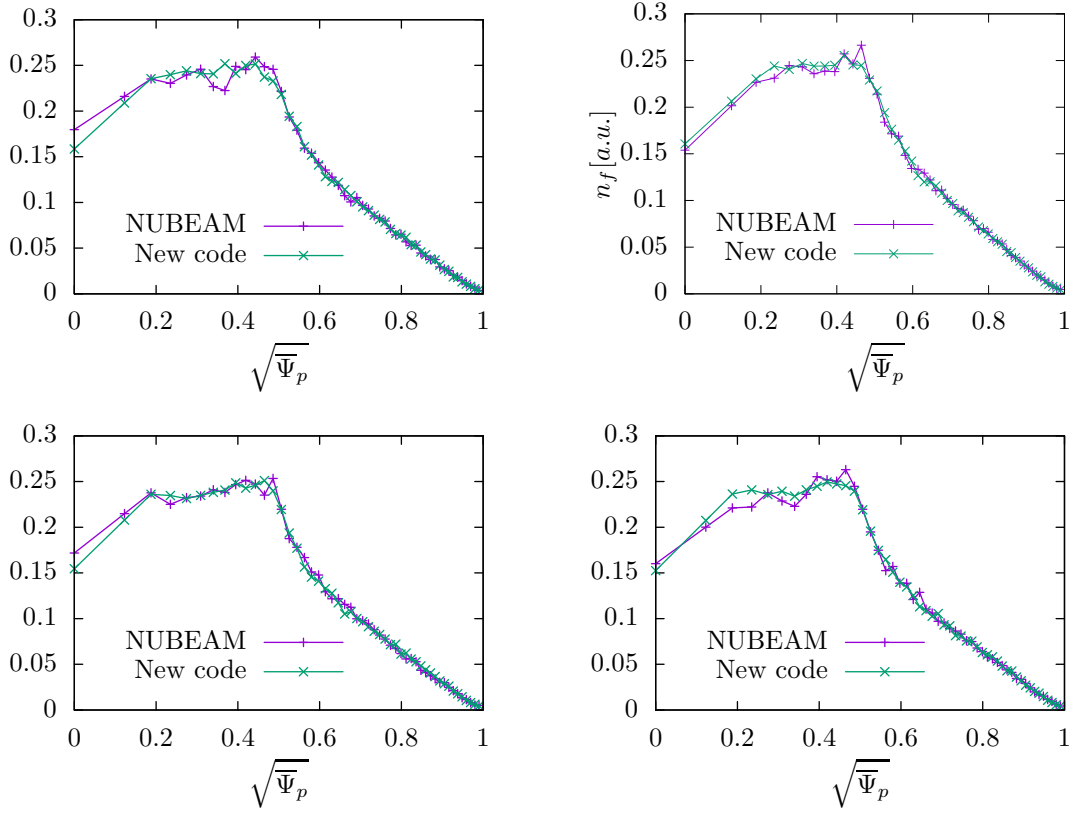
Figure 4. Comparison of flux-surface averaged densities of ionized neutrals calculated by NUBEAM and the new code for EAST discharge #59954@3.0s. Upper left: $R_{\tan} = 0.731m$, upper right: $R_{\tan} = 0.606m$, lower left: $R_{\tan} = 1.264m$, lower right:$R_{\tan} = 1.141m$.

Table 1 compares the shine-through loss given by `TGCO` and `NUBEAM`. The results indicate that good agreement is achieved between the two codes, verifying that the ionization process is accurately modeled in the new code.

	$R_{\tan} = 0.606m$	$R_{\tan} = 0.731m$	$R_{\tan} = 1.141m$	$R_{\tan} = 1.264m$
TGCO	31%	30%	24%	21%
NUBEAM	31%	29%	24%	21%

Table 1. Shine-through loss given by the two codes for different beam tangent radius $R_{\tan}$ in EAST discharge #59954@3.0s.

3.2 Two-dimensional distribution of fast ions

Figure 5 gives the two-dimensional initial poloidal distribution of ionized particles (averaged over the toroidal direction) and toroidal distribution of ionized particles (averaged over the vertical direction). The results indicate that most fast ions are born at the low-field-side for this case.
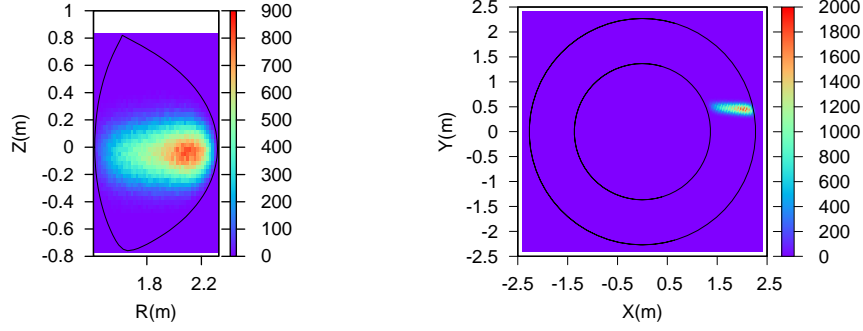
Figure 5. Left: initial distribution of fast ions in the poloidal plane (averaged over the toroidal direction). Right: toroidal distribution of fast ions (averaged over the vertical direction). This is for the neutral beam source with $R_{\text{tan}} = 0.606m$ and for EAST discharge #59954@3.0s.

4 Orbit loss of NBI fast ions

Using the initial distribution of fast ions given by the neutral beam deposition module, the guiding-center orbit or full orbit of each fast ion is followed to check whether it touches the wall. Those touching the wall are considered lost.

4.1 Guiding-center motion

Knowing the birth location $\mathbf{x}$ of a fast ion, the corresponding guiding-center location $\mathbf{X}$ can be calculated via

$$\mathbf{X} = \mathbf{x} + \mathbf{v} \times \frac{\mathbf{b}(\mathbf{x})}{\Omega(\mathbf{x})}, \tag{5}$$

where $\mathbf{v}$ is the fast ion velocity, $\mathbf{b} = \mathbf{B}/B$, $\Omega = BZe/m$ is the cyclotron angular frequency, m and Ze are the mass and charge of the fast ion, respectively, $\mathbf{B}$ is the magnetic field.

The guiding-center orbit of each fast ion is followed numerically. The equations of guiding center motion are given by[11]

$$\frac{d\mathbf{X}}{dt} \equiv \mathbf{v}_d = \frac{\mathbf{B}^\star}{B_\parallel^\star} v_\parallel + \frac{\mu}{m\Omega B_\parallel^\star} \mathbf{B} \times \nabla B + \frac{1}{BB_\parallel^\star} \mathbf{E} \times \mathbf{B}, \tag{6}$$

$$\frac{dv_\parallel}{dt} = -\frac{\mu}{m} \frac{\mathbf{B}^\star}{B_\parallel^\star} \cdot \nabla B + \frac{Ze}{m} \frac{\mathbf{B}^\star}{B_\parallel^\star} \cdot \mathbf{E} \tag{7}$$

where $v_\parallel$ is the parallel (to the magnetic field) velocity, μ is the magnetic moment (a constant of motion) defined by $\mu = mv_\perp^2/(2B)$ with $v_\perp$ being the perpendicular speed; $\mathbf{B}^\star$ and $B_\parallel^\star$ are defined by

$$\mathbf{B}^\star = \mathbf{B} + B\frac{v_\parallel}{\Omega} \nabla \times \mathbf{b}, \tag{8}$$

$$B_\parallel^\star \equiv \mathbf{b} \cdot \mathbf{B}^\star = B\Big(1 + \frac{v_\parallel}{\Omega} \mathbf{b} \cdot \nabla \times \mathbf{b}\Big), \tag{9}$$

respectively; $\mathbf{E}$ is the electrical field; $\mathbf{E} = 0$ in this work.

The cylindrical coordinates are adopted in writing the component equations of guiding-center motion. The 4th order Runge-Kutta scheme is used in integrating the equations. Orbits outside the LCFS are followed until they touch the wall. In the simulation, the magnetic fields in Eqs. (6) and (7) are evaluated at the guiding-center location, i.e., the finite Larmor radius (FLR) effect is ignored. When checking whether a fast ion touches the wall, four points on the gyro-ring are calculated. If any one of the four points touches the wall, the fast ion is considered as lost.

4.2 Orbit loss

For the NBI shine-through loss to be small, most neutral must ionize at the low-field-side (most neutrals ionizing at the the high-field side usually means a very high shine-through loss fraction). As is well known, an ion born at the low-field side with a counter-current initial velocity has an drift orbit that is outside of the magnetic surface where it is born. Therefore this kind of ions are more likely to touch the wall and thus to be lost (an example is given in Fig. 6). This implies that counter-current neutral beam injection usually suffers larger prompt loss than the co-current injection. Figure 7 compares the time evolution of fast ion loss fraction due to counter-current NBI and that due to co-current NBI in EAST discharge #62585@2.8s. The result indicates that the counter-current NBI suffers much higher level of orbit loss.
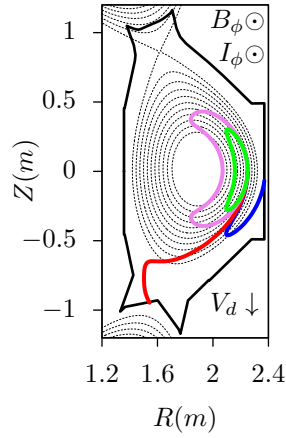
Figure 6. Poloidal orbits of Deuterium particles of 50keV ionized at the low-field-side midplane ($R = 2.25m$, $Z = 0m$) with a birth pitch angle $\theta = 125°$ (red), $\theta = 105°$ (blue), $\theta = 75°$ (green), and $\theta = 65°$ (violet), where the pitch angle θ is the included angle between the magnetic field and the velocity of particles. Since the magnetic field and the plasma current are in the same direction for this case, $\theta > 90°$ means counter-current injection and $\theta < 90°$ means co-current injection. The counter-injected particles are easy to be lost from the plasma because their orbits are outside the flux surface where they are ionized, and thus are more likely to touch the first wall.
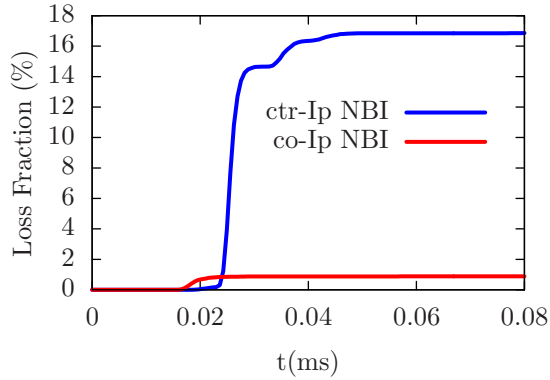

Figure 7. Comparison of fast ions loss fraction due to counter-current NBI and co-current NBI in EAST discharge #62585@2.8s. The central beam is on the midplane with the tangent radius being $0.73m$ and the maximal energy being 50keV.

Figure 8 plots the poloidal distribution of the lost fast ions on the first wall, which shows that fast ions are lost to two regions: the divertor region and the region near the midplane.
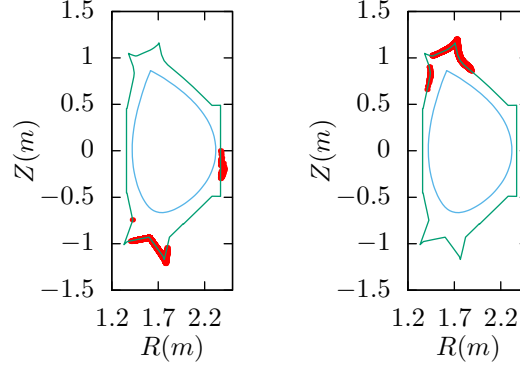

Figure 8. Distribution of the lost fast ions on the first wall for the case $B_\phi < 0$ (left) and $B_\phi > 0$ (right), where B_ϕ is the toroidal component of the magnetic field. Neutral beam is injected in the counter-current injection with $R_{\text{tan}} = 1.26m$. The magnetic configuration is from EAST discharge #62585@2.8s.

As a benchmark, a full orbit integrator using the Boris scheme is also implemented in the code (the details are provided in Appendix B). Figure 9 plots the loss fraction given by the full orbit model and that by the guiding-center model (with the FLR effect included), which shows that the two models agree with each other, giving confidence in the numerical result. If the FLR is neglected when checking whether a fast ion touches the wall, the loss fraction is significantly underestimated, as is shown in Fig. 9.
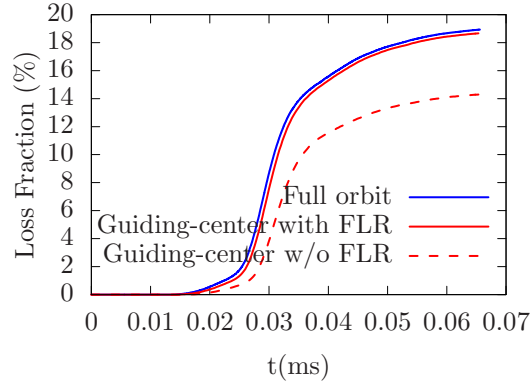

Figure 9. Comparison between results obtained by the full orbit model and guiding-center model. Here guiding-center with FLR means that four points on the gyro-ring are used when checking whether a fast ion touches the wall. This case is a counter-current injection with $R_{\text{tan}} = 0.606m$ for EAST discharge #59954@3s.

5 RMP coils on EAST tokamak and their effect on magnetic field topology

Figure 10 is a sketch map of the RMP coils on EAST tokamak.
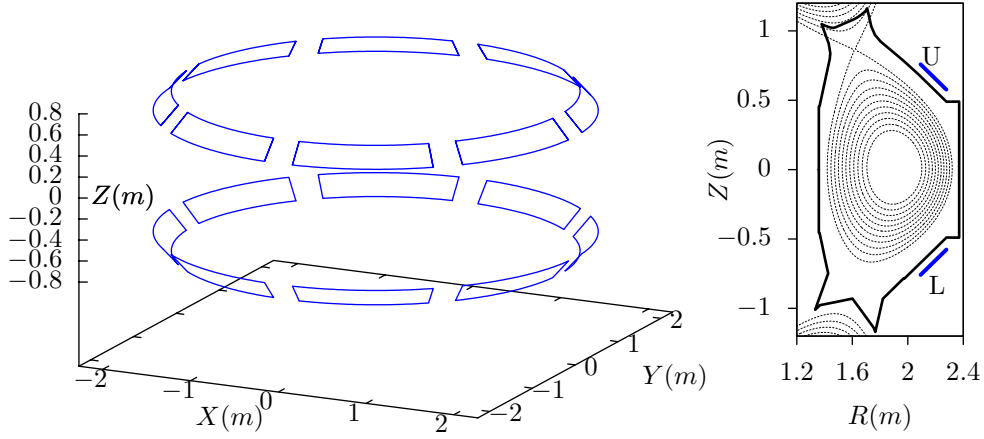
Figure 10. RMP coils on EAST tokamak in 3D view (left) and poloidal view (right). Each coil has 4 turns with maximum current 2.5kA/turn. The maximum frequency of alternating current (AC) operation is 1kHz (usually operating at less than 10Hz). This paper considers only direct current (DC) operation.

Magnetic perturbations produced by the RMP coils are calculated by using the Biot-Savart law. Then the perturbations are superposed on the EFIT equilibrium magnetic field to form the total magnetic field. Figure 11 compares the Poincaré section plots of magnetic field lines without RMP and that with RMP, which shows that magnetic islands and stochastic magnetic region appear in the case with RMP.
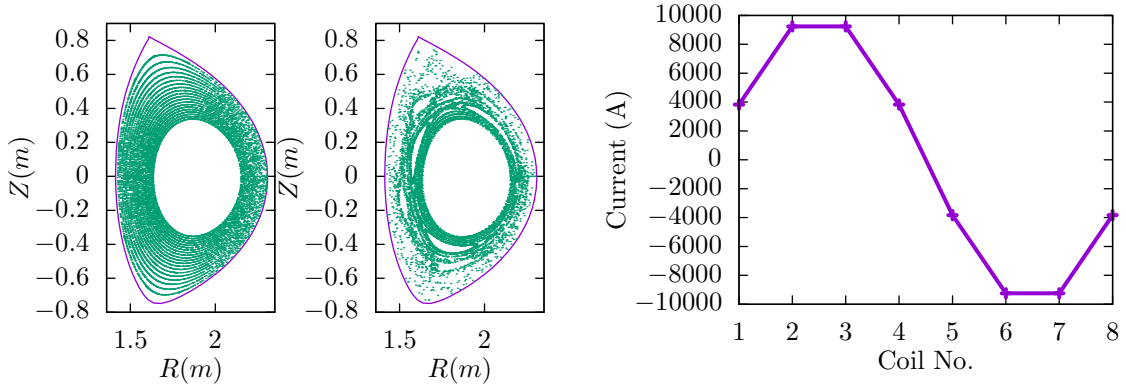

Figure 11. Poincaré section of magnetic field lines of axisymmetric magnetic field (left) and the superposition of the axisymmetric magnetic field and a magnetic perturbation generated by RMP coils (middle). Right: currents in the upper 8 RMP coils (currents in the corresponding lower coils are the same, i.e., upper down symmetric). The currents sample a sine waveform with an amplitude of $1000A$ and a toroidal period of 2π. This is called an $n=1$ RMP. The axisymmetric magnetic field is from EAST discharge #59954@3.1s. These Poincare sections are obtained by tracing 20 field lines starting from 20 points on the the low-field-side midplane, and then then recording the intersecting points of these field lines with the $\phi=0$ plane. The maximum number of intersecting points for each field line is set to 700. In (a), i.e. without RMP, the Poincare points form nested surfaces, which indicates that the accuracy of the field line tracing is enough. In (b), some field lines touch the first wall of the machine before they finish 700 toroidal turns.

6 Prompt loss under the influence of RMP

Figure 12 compares the time evolution of the fast ion loss fraction in the cases with RMP and those without RMP. The results indicate that RMP increases the orbit loss.
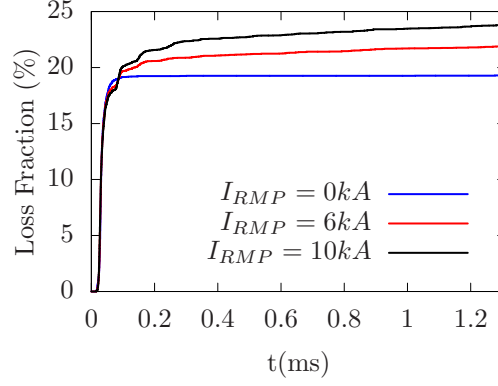

Figure 12. Loss fraction evolution under the influence of an $n = 1$ up-down symmetric RMP. The current indicated is the amplitude of the $n = 1$ sine waveform. This is for a counter-current injection with $R_{\tan} = 0.606m$ in EAST discharge #59954@3.03s.

For the cases with RMP, the loss fractions continue increasing, which is different from the case without RMP, where the loss fraction reaches a steady state. However, the increasing of the loss fraction for the cases with RMP is slow at later time and the loss fraction can be considered to reach a quasi-steady state. Figure 13 plots the dependence of the quasi-steady state loss fraction on the RMP coil current amplitude. The results indicate that the loss fraction is linearly proportional to the current amplitude.
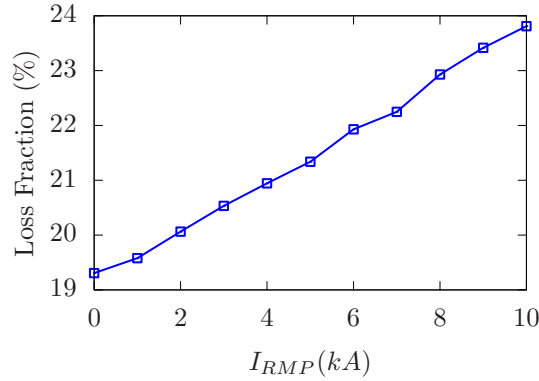

Figure 13. Dependence of the quasi-steady state loss fraction on the RMP coil current amplitude for a waveform with $n = 1$ and up-down symmetry. This is for a counter-current injection with $R_{\tan} = 0.606m$ in EAST discharge #59954@3.03s.

Figure 14 compares the toroidal distribution of lost fast ions without RMP and that with RMP. The results indicate that RMP change the toroidal distribution of lost fast ions.
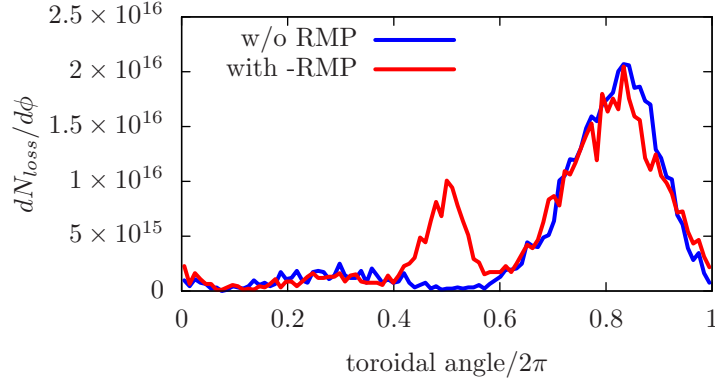
Figure 14. The toroidal distribution of lost fast ions for a counter current injection with $R_{\tan} = 0.606m$ in EAST discharge #59954@3.2s without RMP (blue) and with RMP (red).

7 Summary

A Monte-Carlo code `TGCO` was developed to calculate the neutral beam ionization and fast ions orbit loss under the influence of the 3D magnetic perturbations on EAST tokamak. Numerical results indicate that the 3D magnetic perturbations increase the orbit loss of NBI fast ions and change the toroidal distribution of lost fast ions.

8 ACKNOWLEDGMENTS

Appendix A Ionization cross sections of neutral particles in plasmas

The three ionization cross-sections, namely, cross-section for charge exchange with plasma ions σ_{ch}, cross-section for ionization by plasma ions σ_i , and the effective cross-section of electron impact ionization $\langle \sigma_e v_e \rangle / v_b$, depends on the beam velocity v_b. The effective cross-section of electron impact ionization is special in that it also depends on the temperature of background electrons.

The cross-section for charge exchange with plasma ions σ_{ch} is plotted in Fig. 15 as a function of the kinetic energy per amu (atom mass unit).
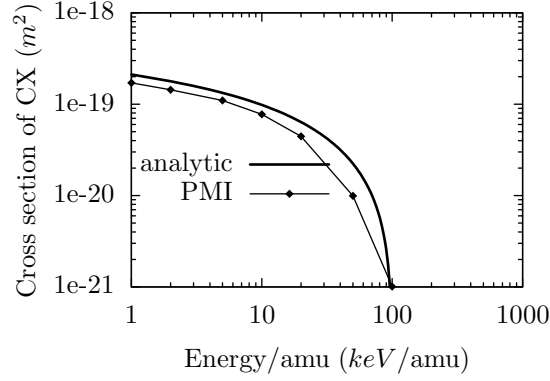
Figure 15. Cross section of charge exchange between Hydrogen-Hydrogen (including the isotopes ^1H, ^2H, and ^3H) as a function of the kinetic energy per amu (atom mass unit). The results labeled by "PMI" is from the data on Page 78 of Ref. [12]. The analytic fitting results (black line) are from Eq. (28) of Ref. [13], which is given by $\sigma_{ex}(m^2) = 10^{-18}(1 - 0.5(2E)^{0.06} + 4 \times 10^{-7}E)$, where E is the collision energy per amu in eV/amu. The values of the fitting cross section agrees with those given in Fig. 5.3.1 of Wesson's book[14].

Kaganovich's paper[15] gives the following fitting formula for the impacting ionization cross section by a fully stripped ion, σ_i:

$$\sigma_i(v, I_{\mathrm{nl}}, Z_p) = \pi a_0^2 \frac{N_{\mathrm{nl}} Z_p^2}{(Z_p + 1)} \frac{E_0^2}{I_{\mathrm{nl}}^2} G^{\mathrm{new}}\left(\frac{v}{v_{\mathrm{nl}}\sqrt{Z_p + 1}}\right), \tag{10}$$

where v is the relative velocity between the atom and the ion, Z_p is the atomic number of the fully stripped ion, I_{nl} is the ionization potential of the atom, $v_{\mathrm{nl}} = v_0\sqrt{2I_{\mathrm{nl}}/E_0}$ with $v_0 = 2.2 \times 10^6 m/s$ and $E_0 = 27.2$eV, N_{nl} is the number of electrons in the nl orbital of the atom ($N_{\mathrm{nl}} = 1$ for hydrogen), $a_0 = 0.529 \times 10^{-10}m$ is the Bohr radius, and $G^{\mathrm{new}} = x^{-2}\exp(-x^{-2})[1.26 + 0.283\ln(2x^2 + 25)]$.
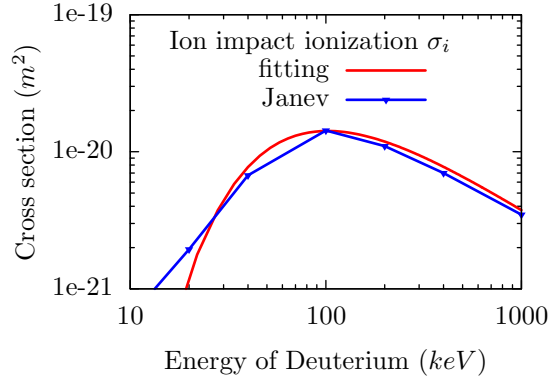

Figure 16. Cross section of ion impact ionization of deuterium as a function of the kinetic energy of deuterium atom (red line is calculated by using Eq. (10), data of blue line are from the data on Page 68 of Ref. [12]).

For neutral beam injection relevant to present tokamaks, the thermal velocity of plasma ions are much smaller than the velocity of beam atoms, i.e., $v_{ti} \ll v_b$, so that $v_{ti} \approx 0$ can be assumed. As a result, σ_{ch} and σ_i discussed above are independent of the temperature of the background plasma ions. However, the electron impact ionization rate coefficient $\langle\sigma_e v_e\rangle$ usually depends on the temperature of background electrons because the thermal velocity of electrons is usually comparable to the beam velocity and an averaging over the electron Maxwellian distribution is needed. The dependence of the electron ionization rate coefficient $\langle\sigma_e v_e\rangle$ on the electron temperature is plotted in Fig. 17.
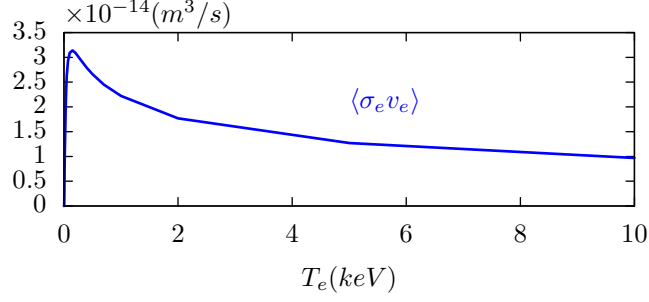
Figure 17. The dependence of the electron impact ionization rate coefficient $\langle \sigma_e v_e \rangle$ on the electron temperature T_e. These data are obtained by using the open-ADAS reading program "xxdata_07" to acces the ADAS data file "szd93#h_h0.dat", which stores the electron ionization rate coefficient for hydrogen atom.

Knowing $\langle \sigma_e v_e \rangle$, the electron impact ionization cross section is given by $\langle \sigma_e v_e \rangle / v_b$, where v_b the velocity of beam particles. Fig. 18 plots the dependence of the electron impact ionization cross section on the kinetic energy of Deuterium atom for different background electron temperatures.
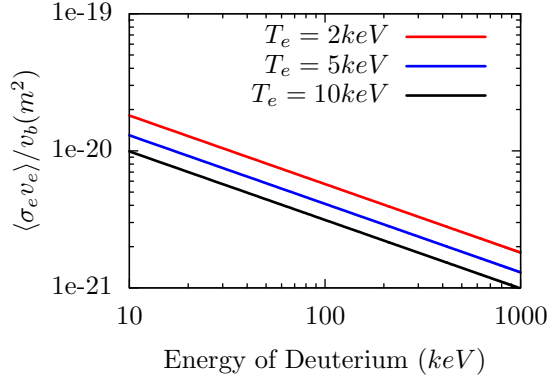

Figure 18. The dependence of the electron impact ionization cross section $\langle \sigma_e v_e \rangle / v_b$ on the kinetic energy of Deuterium atom for the three cases with $T_e = 2\mathrm{keV}$, $5\mathrm{keV}$, and $10\mathrm{keV}$.

In this work, the analytical fitting formula for the cross-sections are not used in the simulations. The simulations directly use numerical spline interpolation to obtain the values of the cross-sections from the data provided in Janev's paper[12] and the ADAS database (https://open.adas.ac.uk/).

Appendix B Full orbit integrator

The full orbit is advanced by a time-centered difference scheme given by

$$\frac{\mathbf{v}^{(n+1/2)} - \mathbf{v}^{(n-1/2)}}{\Delta t} = \frac{q_i}{m_i} \left[\mathbf{E}^{(n)}(\mathbf{x}^{(n)}) + \frac{\mathbf{v}^{(n+1/2)} + \mathbf{v}^{(n-1/2)}}{2} \times \mathbf{B}^{(n)}(\mathbf{x}^{(n)}) \right]. \tag{11}$$

for velocity and

$$\frac{\mathbf{x}^{(n+1)} - \mathbf{x}^{(n)}}{\Delta t} = \mathbf{v}^{(n+1/2)}, \tag{12}$$

for position. Here staggered time grids are used for $\mathbf{v}$ and $\mathbf{x}$: time grids of $\mathbf{v}$ are at half-steps while time grids of $\mathbf{x}$ are at integer steps. The scheme given in Eq (11) is in an implicit form since the unknown $\mathbf{v}^{(n+1/2)}$ appears on both sides of the equation. Fortunately, equation (11) can be analytically solved in Cartesian basis and its explicit solution is expressed by the Boris algorithm[16]. In this work, cylindrical coordinates are used in integrating full orbits. When implementing the Boris scheme in cylindrical coordinates, a local Cartesian coordinate system with basis vectors $(\mathbf{e}_x, \mathbf{e}_y, \mathbf{e}_z)$ along the local cylindrical basis vectors $(\mathbf{e}_R, \mathbf{e}_\phi, \mathbf{e}_Z)$ at particle location $\mathbf{x}^{(n)}$ is set up to perform the velocity integration to obtain $\mathbf{v}^{(n+1/2)}$. Then the particle location is updated in the local Cartesian coordinates by using Eq. (12) and then is transformed to the cylindrical coordinates by using the analytic coordinate transformation. After this, the new velocity $\mathbf{v}^{(n+1/2)}$ is projected onto the new basis vectors $(\mathbf{e}_R, \mathbf{e}_\phi, \mathbf{e}_Z)$ at particle location $\mathbf{x}^{(n+1)}$. This scheme can reproduce correct drift motion even when a large time-step comparable to the gyro-period is used[17, 18].

Bibliography

[1]   J.T. Scoville, M.D. Boyer, B.J. Crowley, N.W. Eidietis, C.J. Pawley, and J.M. Rauch. New capabilities and upgrade path for the diii-d neutral beam heating system. *Fusion Engineering and Design*, 146:6 − 9, 2019. SI:SOFT-30.

[2]   Chundong Hu, Yahong Xie, Yuanlai Xie, Sheng Liu, Yongjian Xu, Lizhen Liang, Caichao Jiang, Peng Sheng, Yuming Gu, Jun Li, and Zhimin Liu. Overview of development status for EAST-NBI system. *Plasma Science and Technology*, 17(10):817–825, oct 2015.

[3]   M. Schneider, L.-G. Eriksson, I. Jenkins, J.F. Artaud, V. Basiuk, F. Imbeaux, T. Oikawa, and and. Simulation of the neutral beam deposition within integrated tokamak modelling frameworks. *Nuclear Fusion*, 51(6):063019, may 2011.

[4]   O. Asunta, J. Govenius, R. Budny, M. Gorelenkova, G. Tardini, T. Kurki-Suonio, A. Salmi, and S. Sipilä. Modelling neutral beams in fusion devices: Beamlet-based model for fast particle simulations. *Computer Physics Communications*, 188:33 − 46, 2015.

[5]   W W Heidbrink, M Murakami, J M Park, C C Petty, M A Van Zeeland, J H Yu, and G R McKee. Beam-ion confinement for different injection geometries. *Plasma Physics and Controlled Fusion*, 51(12):125001, oct 2009.

[6]   Bin Wu, Baolong Hao, Roscoe White, Jinfang Wang, Qing Zang, Xiaofeng Han, and Chundong Hu. Calculation of prompt loss and toroidal field ripple loss under neutral beam injection on EAST. *Plasma Physics and Controlled Fusion*, 59(2):025004, dec 2016.

[7]   Y. Sun, M. Jia, Q. Zang, L. Wang, Y. Liang, Y.Q. Liu, X. Yang, W. Guo, S. Gu, Y. Li, B. Lyu, H. Zhao, Y. Liu, T. Zhang, G. Li, J. Qian, L. Xu, N. Chu, H.H. Wang, T. Shi, K. He, D. Chen, B. Shen, X. Gong, X. Ji, S. Wang, M. Qi, Q. Yuan, Z. Sheng, G. Gao, Y. Song, P. Fu, and B. Wan and. Edge localized mode control using n = 1 resonant magnetic perturbation in the EAST tokamak. *Nuclear Fusion*, 57(3):036007, dec 2016.

[8]   Yingfeng Xu, Wenfeng Guo, Youjun Hu, Lei Ye, Xiaotao Xiao, and Shaojie Wang. Monte carlo orbit-following simulations including the finite larmor radius effect based on a phase-space coordinate transform method. *Computer Physics Communications*, 244:40 − 48, 2019.

[9]   Alexei Pankin, Douglas McCune, Robert Andre, Glenn Bateman, and Arnold Kritz. The tokamak monte carlo fast ion module nubeam in the national transport code collaboration library. *Computer Physics Communications*, 159(11):157–184, 2004.

[10]   L.L. Lao, H. St. John, R.D. Stambaugh, A.G. Kellman, and W. Pfeiffer. Reconstruction of current profile parameters and plasma shapes in tokamaks. *Nucl. Fusion*, 25(11):1611, 1985.

[11]   Y. Todo. Properties of energetic-particle continuum modes destabilized by energetic ions with beam-like velocity distributions. *Phys. Plasmas (1994-present)*, 13(8):–, 2006.

[12]   R. K. Janev and J. J. Smith. Cross sections for collision processes of hydrogen atoms with electrons, protons and multiply charged ions. *Atomic and Plasma-material Interaction Data for Fusion*, 4, 1993.

[13]   O. Demokan and V. Mirnov. Rigorous treatment of charge exchange, ionization, and collisional processes in neutral-beam-injected mirrors. *Physics of Plasmas*, 2(1):139–145, 1995.

[14]   John Wesson. *Tokamaks*. Oxford University Press, 2004.

[15]   Igor D. Kaganovich, Edward A. Startsev, and Ronald C. Davidson. Scaling cross sections for ion-atom impact ionization. *Physics of Plasmas*, 11(3):1229–1232, 2004.

[16]   C.K. Birdsall and A.B Langdon. *Plasma Physics via Computer Simulation*. CRC Press, 2004.

[17]   S.E Parker and C.K Birdsall. Numerical error in electron orbits with large $\omega_{ce}\,\delta\,t$. *Journal of Computational Physics*, 97(1):91 − 102, 1991.

[18]   Youjun Hu, Matthew T. Miecnikowski, Yang Chen, and Scott E. Parker. Fully kinetic simulation of ion-temperature-gradient instabilities in tokamaks. *Plasma*, 1(1):105–118, 2018.